Supplemental Information for

Reinforcing the Symmetry of Stripping/plating Behavior via *In-situ* Interface Construction for Long-lasting Zinc Metal Batteries

Dongmin Li,[a] Yunpeng Zhong,[a] Xieyu Xu,[b] Daren Zhou,[a] Yan Tang,[a] Liangbing Wang,[a] Shuquan Liang,[a] Bingan Lu,[c] Yangyang Liu,[b] and Jiang Zhou*[a]*

[a] School of Materials Science & Engineering, Hunan Provincial Key Laboratory of Electronic Packaging and Advanced Functional Materials of Hunan Province, Central South University, Changsha 410083, China, E-mail: zhou_jiang@csu.edu.cn

[b] State Key Laboratory for Mechanical Behavior of Materials, Xi′an Jiaotong University, Xi′an 710049, China, E-mail: liuyy0510@xjtu.edu.cn

[c] School of Physics and Electronics, Hunan University, Changsha 410082, China.

Experimental Section

Materials

Zinc perchlorate hexahydrate ($Zn(ClO_4)_2 \cdot 6H_2O$, AR), N, N'-Dimethylpropyleneurea (DU, AR), and N-methyl pyrrolidone (NMP, AR) were purchased from Shanghai Macklin Biochemical Technology Co., Ltd. Ammonium metavanadate (NH_4VO_3, AR) was purchased from Shanghai Aladdin Biochemical Technology Co., Ltd. Ethanedioic acid dihydrate ($H_2C_2O_4 \cdot 2H_2O$, GR) was purchased from Sinopharm Chemical Reagent Co., Ltd. Super P (cell grade) and polyvinylidene fluoride (PVDF, cell grade) were purchased from Soochow DoDoChem Technology Co., Ltd. All chemicals were used as received without any further purification.

Electrolyte preparation

A series of electrolytes was formulated by dissolving 2 M $Zn(ClO_4)_2$ in deionized (DI) water with different volume ratios of H_2O/DU from 1:0, 4:1, 3:2, 2:3, 1:4 to 0:1. The corresponding electrolyte is marked as BE, 8H2D, 6H4D, 4H6D, 2H8D, and DU electrolyte, respectively.

Synthesis of $NH_4V_4O_{10}$ cathode

1.170 g NH_4VO_3 and 1.891 g $H_2C_2O_4 \cdot 2H_2O$ were mixed into 35 mL DI water and stirred at 80 °C to dissolve completely. The above mixed solution was transferred to a 50 mL Teflon autoclave and heated in an oven at 140 °C for 48 hours. The filtration-collected material was washed repeatedly with DI water and dried in a vacuum oven at 90 °C for 12 hours.

Material characterizations

Nuclear magnetic resonance (NMR, Bruker Avance NEO 400 MHz) and Fourier-transform infrared spectroscopy (FT-IR, Thermo Nicolet iS50) were used to investigate the electrolyte information. Dataphysics (Lauda Scientific LSA100) was tested for wettability between electrolyte and anode. The crystallographic phases involved were analyzed by X-ray diffraction (XRD, Rigaku Mini Flex 600) measurements with a Cu-target X-ray tube (λ = 0.15405 nm). Scanning electron microscopy (SEM, MIRA3 TESCAN), energy dispersive spectrometer (EDS), optical microscope (LW750LJT), atomic force microscope (AFM, Bruker Dimension

Icon), and transmission electron microscopy (TEM, Titan G2 60-300) were performed to characterize the morphology of samples. X-ray photoelectron spectroscopy (XPS, Thermo Scientific K-Alpha) was used to investigate the sample valence bond information. Zeta potential measurement was conducted using Malvern Zetasizer Nano ZS90.

Electrochemical measurements

Cyclic voltammetry (CV), electrochemical impedance spectroscopy (EIS), liner sweep voltammetry (LSV), liner polarization (or Tafel) curve, chronoamperometry (CA), alternating current (AC) voltammetry, and galvanostatic charge−discharge (GCD) were performed utilizing electrochemical station (CHI660E) and LAND cell tester (LAND CT2001A). For cycling stability of Zn||Zn symmetric batteries, 2025-type coin cells were assembled with Zn foil as cathode and anode, glass fibers (Whatman GF/D) as diaphragm, and different electrolytes. For Coulomb efficiency (CE) tests of Zn plating/stripping, titanium foil served as the working electrode and Zn foil as the counter electrode. The charging cut-off voltage is 0.5 V. For galvanostatic cycling of $NH_4V_4O_{10}$||Zn full cells, Zn foil was used as the anode and $NH_4V_4O_{10}$ electrode was used as the cathode. The voltage window was set to 0.4−1.4V. For the $NH_4V_4O_{10}$ electrode, the as-prepared $NH_4V_4O_{10}$, super P, and PVDF were mixed with a 7:2:1 ratio in NMP to form a slurry, which was coated on stainless steel mesh or carbon cloth (for high load test) with a diameter of 12 mm and then dried in a vacuum oven. The mass of the active material was approximately, 1.0−1.5 mg cm^{-2} (routine test), 4.2−4.3 mg cm^{-2} (low N/P ratio test), and 10.47 mg cm^{-2} (pouch cell), respectively. The thickness of the Zn foil is 100 μm, excluding cells with high depth of discharge (DoD, 10 μm) and a certain N/P ratio (adjusted according to the capacity of the cathode electrode). For the solar charging test, $NH_4V_4O_{10}$||Zn pouch cell and typical silicon solar cell were in series. For the EIS measurements, the applied frequency range was from 10^5 Hz to 10^{-2} Hz.

Computational methods

Multi-physics simulation

Multi-physics simulation model for the electrodeposition of Zn metal was built in COMSOL Multiphysics 6.0 software, primarily involving electrochemical reactions (using the classical

Butler-Volmer equation and Faraday's electrolysis law), the Nernst-Einstein relationship considering the influence of Faradic electric fields, and three-dimensional dynamic simulation of stripping and deposition process of Zn metal.[1-4] **(1) Surface Roughness:** The Zn metal anode surface exhibits a certain surface roughness, with an average roughness of 19.86 μm, and dimensions of 100×100 μm². This roughness can be implemented in COMSOL using Gaussian random and uniform random distribution functions. **(2) Meshing:** Ultrafine meshing was employed, with a maximum grid size of 0.015 μm, to accurately capture the influence of the interfacial electric field and concentration of Zn^{2+} on the dynamically evolving surface of Zn metal. COMSOL's deformation mesh functionality was utilized to dynamically simulate the effect of changing electric fields on mass transport during the electrodeposition of Zn. This is crucial for accurately simulating real-world electrode processes. **(3) Solver and Settings:** The MUMPS solver was used to handle the model-solving process. In the model, it was assumed that the electrodeposition efficiency is 100%, hence no secondary reactions are considered.

Ab initial calculations

All first principle calculation (Ab initio) calculations were accomplished using the Vienna Ab initio simulation package (VASP).[5, 6] The generalized gradient approximation (GGA) functionals were considered by PerdewBurke-Ernzerh as well as the projector augmented wave method (PAW-PBE) to describe exchange-correlation effects between electrons.[7-9] 20.0 Å vacuum layer was introduced on the Z-axis direction to limit interactions between periodic images. The energy cutoff for the plane-wave basis set was 520 eV. In the optimization process, the convergence criterion for the electronic self-consistent field (SCF) and loop was set to 1×10^{-6} eV/atom, in the single energy process the convergence criterion for the electronic SCF and loop was set to 1×10^{-8} eV/atom. All the structures are relaxed until the residual forces on the atoms have declined to less than 0.02 eV/Å. For all calculations, Van der Waals interaction was taken into account at DFT-D4.[10] The adsorption energy is calculated via: $E_{ads}= E_{Zn+\ mol}- E_{Zn}- E_{mol}$, where the $E_{Zn+\ mol}$, the E_{Zn}, and the E_{mol} represent the total energy of adsorbates on the Zn surface, the energy of Zn surface, and the energy of the isolated adsorbates, respectively.

Quantum chemistry calculations

The density functional theory (DFT) method was performed using the Gaussian16 program.

The M06-2X-D3/ma-TZVP theoretical model was adopted for the structural optimizations and the M06-2X-D3/ma-QZVP relative energy calculations.[11, 12] The binding energy (E_{bind}) between the Zn^{2+}-solvent pairs and anion is defined as: $E_{bind} = E_{cluster} - E_A - E_B$, where $E_{cluster}$, E_A, and E_B represent the total energy of the clusters, free A, and free B, respectively. The molecular frontline orbitals were analyzed and plotted by the graphical interface of GaussView6.1. and VMD.[13]

Molecular dynamics simulation

The molecular dynamics simulations were performed using the LAMMPS package.[14] The OPLS-AA force field was selected in this work, which is good for the investigation of various small organic molecules.[15] Water molecules were simulated with the SPC/E model. The partial charges on atoms were obtained using the restrained electrostatic potential (RESP) method which was calculated with Multiwfn software.[16, 17] Our modeling system contains 2276 H_2O and 150 $Zn(ClO_4)_2$ for system 1 and 522 H_2O, 150 $Zn(ClO_4)_2$ and 310 DU for system 2. The electrolyte system was initialized using the Packmol package and the Moltemplate package.[18, 19] The periodic boundary conditions were conducted in the x, y, and z directions. A cutoff distance of 1.2 nm was used in the calculation of electrostatic interactions. The temperature and pressure coupling were performed in Nose-Hoover and Berendsen methods, respectively.

Fig.s and captions

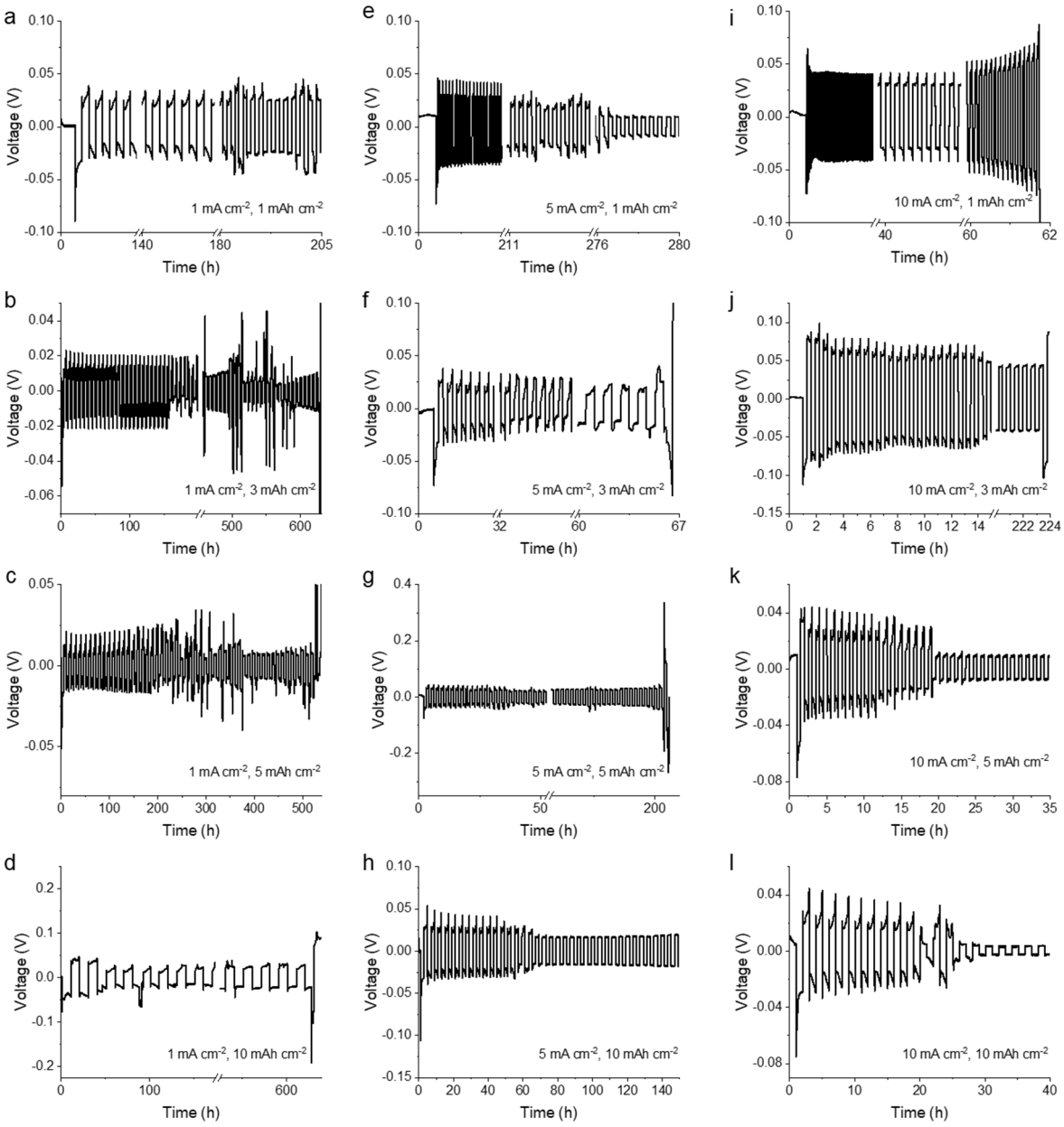

Fig. S1. Voltage profiles at different currents and capacities. Voltage profiles of Zn||Zn cells at (a) 1 mA cm^{-2} and 1 mAh cm^{-2}, (b) 1 mA cm^{-2} and 3 mAh cm^{-2}, (c) 1 mA cm^{-2} and 5 mAh cm^{-2}, (d) 1 mA cm^{-2} and 10 mAh cm^{-2}, (e) 5 mA cm^{-2} and 1 mAh cm^{-2}, (f) 5 mA cm^{-2} and 3 mAh cm^{-2}, (g) 5 mA cm^{-2} and 5 mAh cm^{-2}, (h) 5 mA cm^{-2} and 10 mAh cm^{-2}, (i) 10 mA cm^{-2} and 1 mAh cm^{-2}, (j) 10 mA cm^{-2} and 3 mAh cm^{-2}, (k) 10 mA cm^{-2} and 5 mAh cm^{-2}, and (l) 10 mA cm^{-2} and 10 mAh cm^{-2}.

The stripping/plating behavior is summarized. In the polarization zone, the

plating/stripping of the Zn electrode is relatively flat and the inevitable side reactions occur at the Zn electrode-electrolyte interface. The accumulation of by-products and electrolyte depletion lead to a drastic rise in the polarization voltage, which ultimately makes the cell failure. Interfacial protection strategies can be implemented to inhibit water-induced side reactions. The transition zone is located between the polarization and short-circuit zones, indicating that Zn dendrites can pierce the separator to make a localized electrical connection between the two electrodes. In the short-circuit zone, the synergistic effects of uneven stripping/plating make it inevitable for dendrites to pierce the separator. In the asymmetry zone, the asymmetric voltage of stripping/plating is followed by an atypical galvanostatic voltage response, which indicates that the asymmetry of stripping/plating is directly related to cell failure. In the transition zone, the stripping/plating voltage can be asymmetrical during the cycling process, and the asymmetry of stripping/plating is a potential contributor to cell failure. In the symmetry zone, the stripping/plating voltage remains symmetrically stable throughout the cycle. It is noted that at a fixed low capacity (1 mAh cm^{-2}), the lifetime of the cell prolongs before the current density increases to 5 mAh cm^{-2}, which could be ascribed to the turn of the stripping/plating process towards kinetic control prolonging the lifetime.[20] Overall, the lifespan of the cell tends to shorten with increasing current density and capacity.

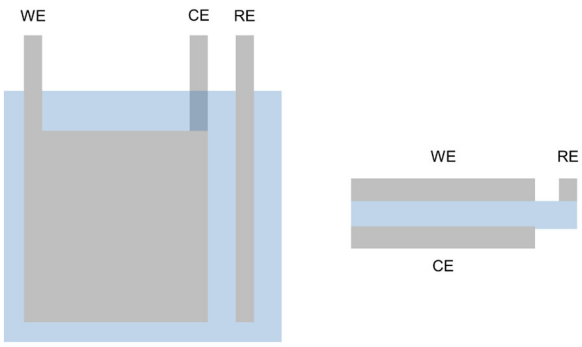

Fig. S2. Three electrode cell schematics (WE, Zn working electrode; RE, Zn reference electrode; CE, Zn counter electrode).

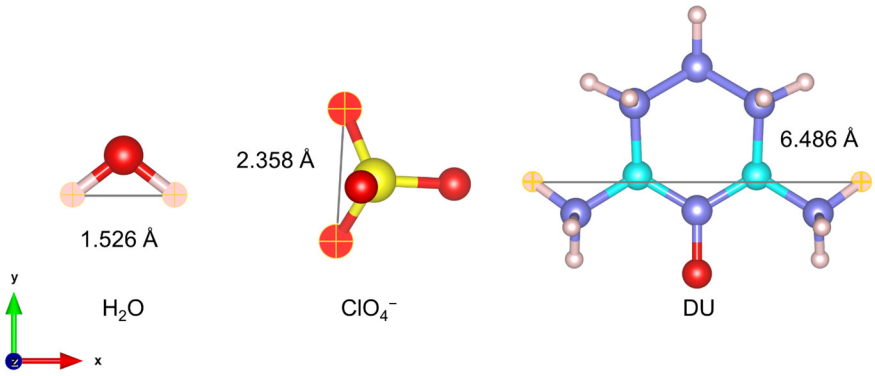

Fig. S3. Dimensional comparison of H_2O, ClO_4^- and DU.

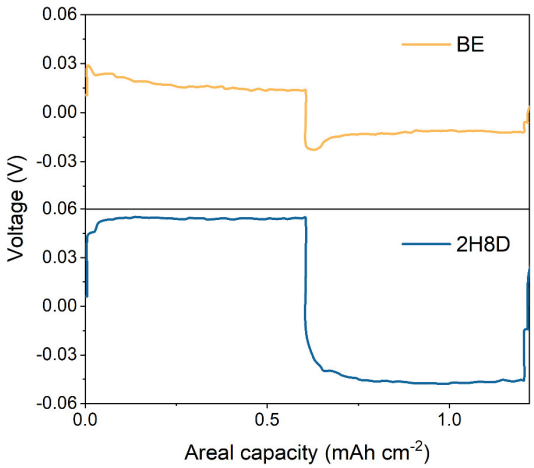

Fig. S4. Voltage profile of Zn electrodes stripping/plating in different electrolytes at 5 mA cm^{-2} and 3 mAh cm^{-2}.

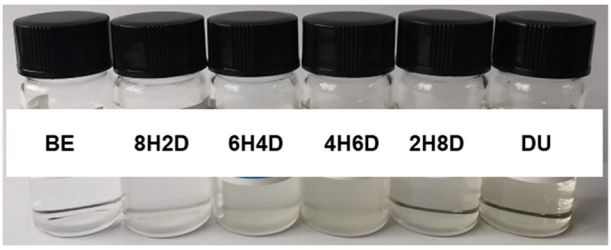

Fig. S5. The photographs of hybrid electrolytes with different DU contents.

The hybrid electrolyte is a homogeneous and transparent liquid when DU and water are mixed in a predetermined volume ratio of greater than 4:1.

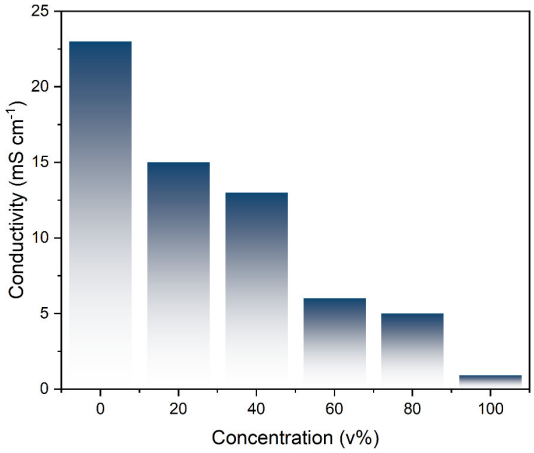

Fig. S6. Ionic conductivities of hybrid electrolytes with different DU contents.

The ionic conductivity of the hybrid electrolyte was measured by testing the impedance of a symmetric coin cell. The equation for calculating ionic conductivity is as follows:

$$\sigma = \frac{\mathrm{L}}{\mathrm{R} \cdot \mathrm{A}}$$

where σ represents the ionic conductivity of the electrolyte, L represents the distance between two electrodes, R represents the electrolyte resistance, and A represents the area of the electrode. The ionic conductivity of the electrolytes decreases with rising ratios of DU, which could be ascribed to the elevated viscosity of the electrolytes. The water in the hybrid electrolyte guarantees that the ionic conductivity of the 2H8D electrolyte reaches 5 mS cm^{-1}, which is an order of magnitude closer to the BE electrolyte.

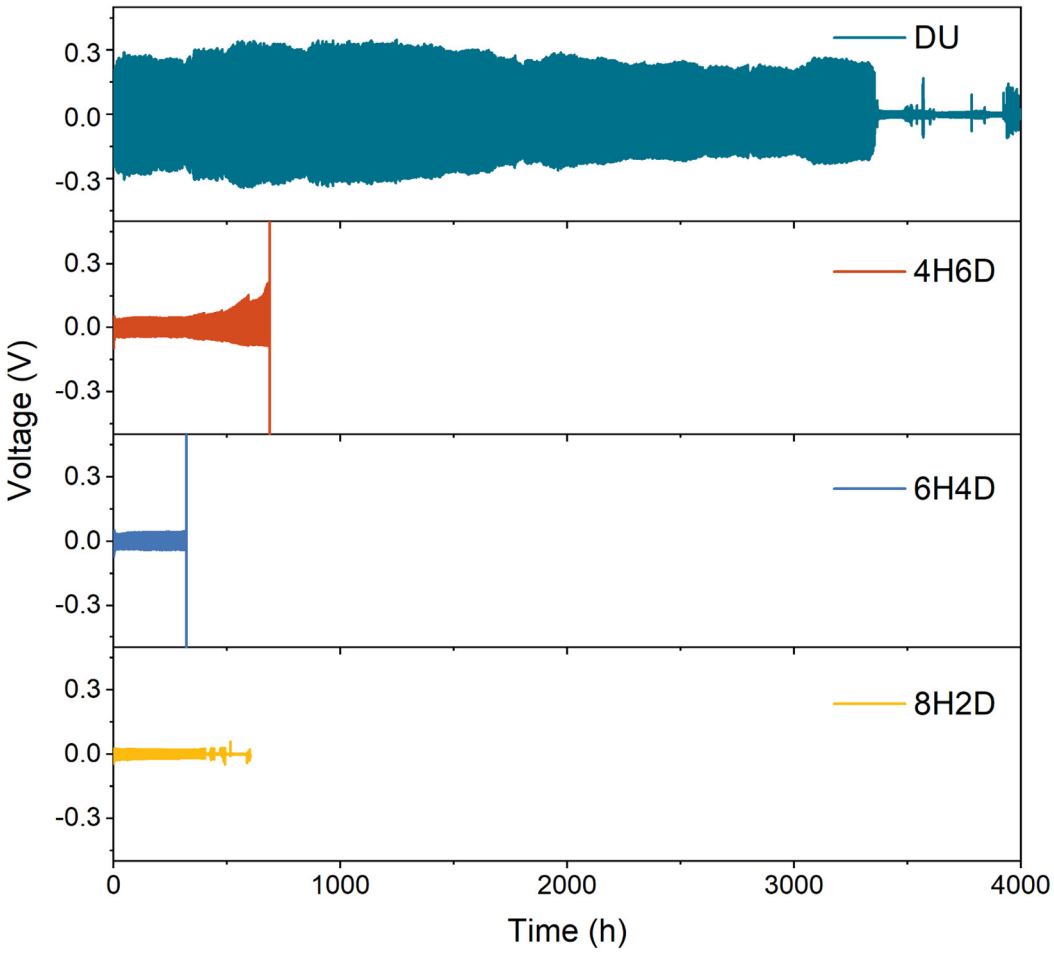

Fig. S7. Galvanostatic cycling stability of Zn||Zn symmetric cells in different electrolytes at 1 mA cm^{-2} and 1 mAh cm^{-2}.

Zn||Zn symmetric cells are used to investigate DU content for reversibility and stability of Zn anodes. For cells using the 8H2D, 6H4D, and 4H6D electrolytes, stable cycles of approximately 387 hours, 321 hours, and 689 hours are obtained, respectively. Electrochemical performance using these electrolytes shows irregular variations regarding DU content, which corresponds to unstable electrolytes in a predetermined ratio range (volume ratio of H_2O/DU=4:1−2:3). The hysteresis voltage increases with increasing DU content, which could be attributed to the increased viscosity of the electrolyte. Notably, the cell using DU electrolyte without H_2O exhibits a stable lifetime over 3355 hours, which indicates the beneficial effect of DU in improving the Zn anode stripping/plating behavior. However, the excessive polarization is mainly attributed to the reduced ionic conductivity and sluggish kinetics.

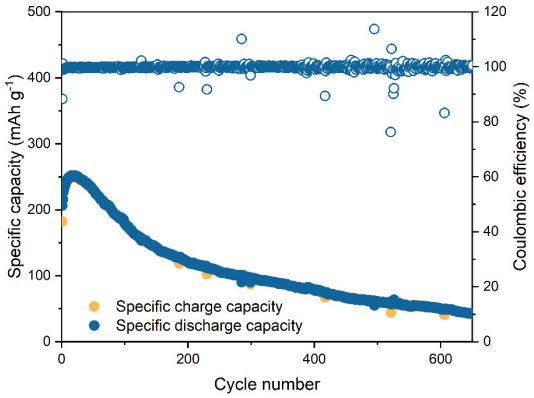

Fig. S8. Cycling performance of $NH_4V_4O_{10}$||Zn cells at 0.5 A g^{-1} in DU electrolyte without H_2O.

The reduced capacity and poor cycling stability of $NH_4V_4O_{10}$||Zn full cell indicate that H_2O serves as a pivotal transport medium for reversible Zn^{2+} insertion, notwithstanding its detrimental effects on cell stability. The 2H8D electrolyte exhibits the optimal performance based on a comprehensive evaluation in terms of electrolyte stability (**Fig. S5**), ionic conductivity (**Fig. S6**), and cycling stability of the symmetric and full cells (**Fig. S7, 8**). Therefore, 2H8D electrolyte was chosen for this work.

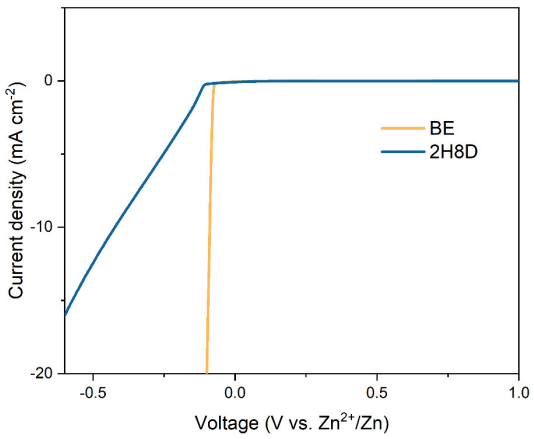

Fig. S9. LSV curves of BE and 2H8D electrolytes at a scan rate of 2 mV s^{-1}.

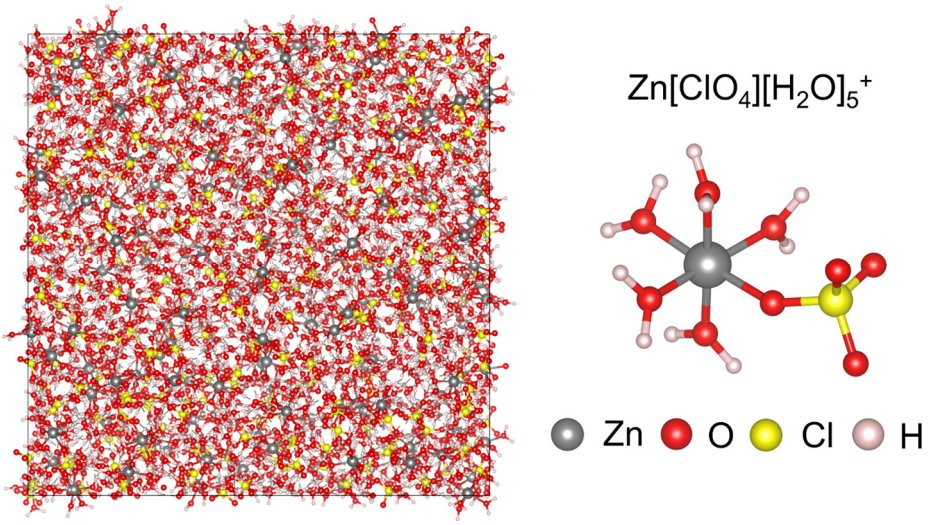

Fig. S10. 3D snapshot of BE electrolyte obtained from MD simulation.

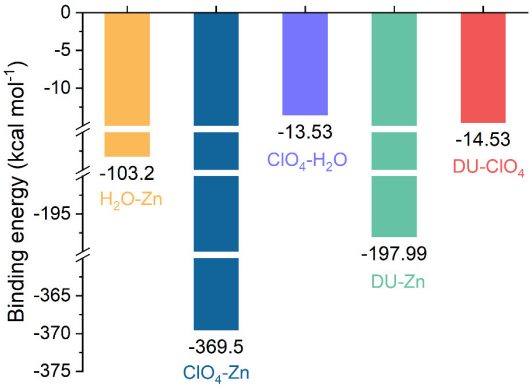

Fig. S11. Binding energies of H_2O−Zn, ClO_4−Zn, ClO_4−H_2O, DU−Zn, and DU−ClO_4.

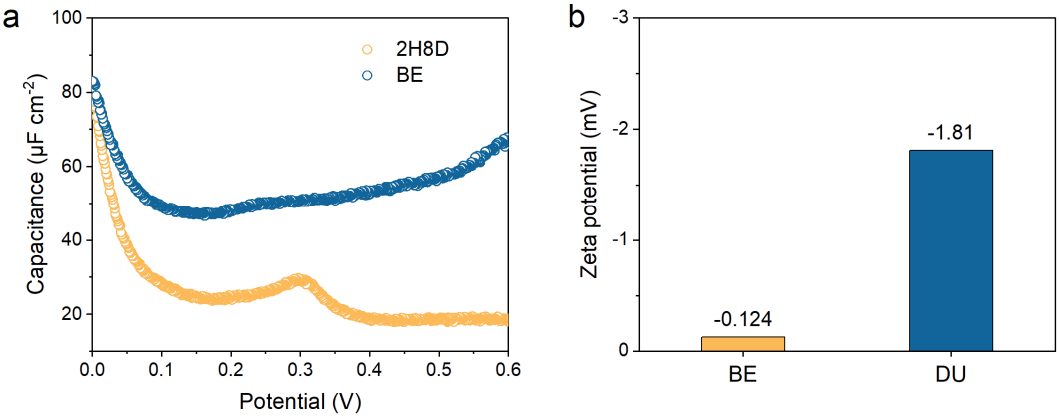

Fig. S12. (a) The differential capacitance curves of cells with BE and 2H8D electrolytes. **(b)** Zeta potential measurement of Zn metal.

The potential zero charge (PZC), defined as the potential at which no excess charge exists on the surface, represents a scenario in which the surface capacitance is minimum. And PZC is also used as an indicator of the structural evolution of the electric double-layer. The adsorption of positively charged species typically results in a shift of the PZC towards more negative potentials, whereas the adsorption of negatively charged species leads to a more positive shift.[21, 22]

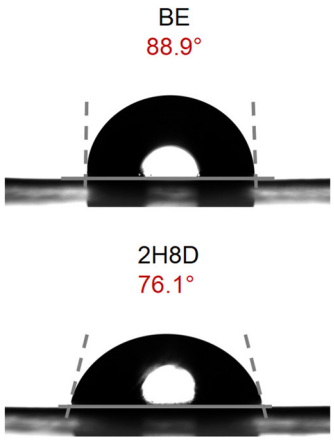

Fig. S13. Optical images of contact angles between Zn foil and BE (top), and 2H8D (bottom), respectively.

The contact angle between the Zn surface and electrolyte was measured, in which the decreased contact angle for the 2H8D electrolyte indicates that the DU exerts a positive influence on the wettability of the Zn anode.

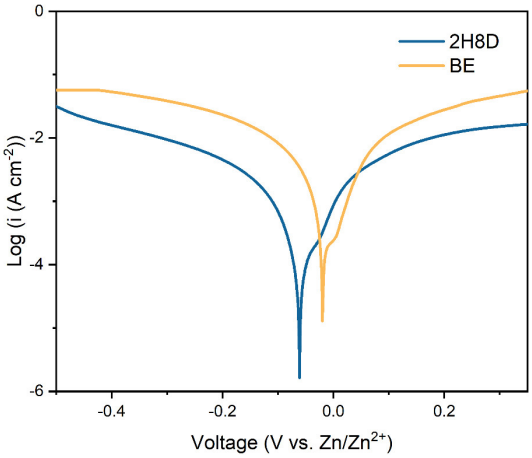

Fig. S14. Tafel polarization curves of BE and 2H8D electrolytes.

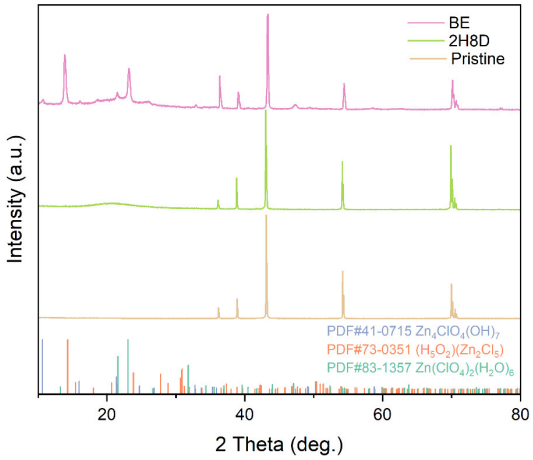

Fig. S15. XRD patterns of Zn foil soaked in BE and 2H8D electrolytes.

After the Zn foil was immersed in BE electrolyte for 14 days, the intense diffraction peaks of the by-products appeared from the XRD pattern, even rivaling the peaks of Zn, which indicates that the side reaction persists violently on the Zn surface. In contrast, only negligible peaks of by-products show on the surface of the Zn foil in the 2H8D electrolyte. These results indicate that the 2H8D electrolyte effectively suppresses the HER and improves the corrosion resistance of the aqueous electrolyte.

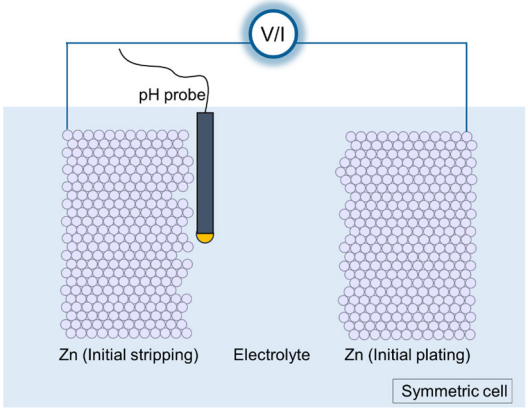

Fig. S16. Schematic diagram of *in-situ* pH monitoring. The probe was located close to the IS-Zn electrode possible.

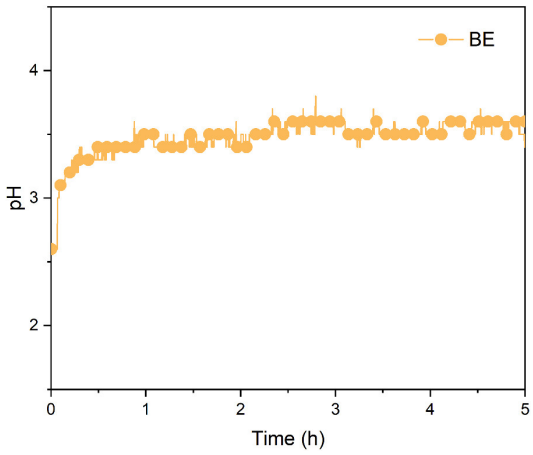

Fig. S17. The pH value detection of BE electrolyte near the IS-Zn electrode in Zn||Zn cell.

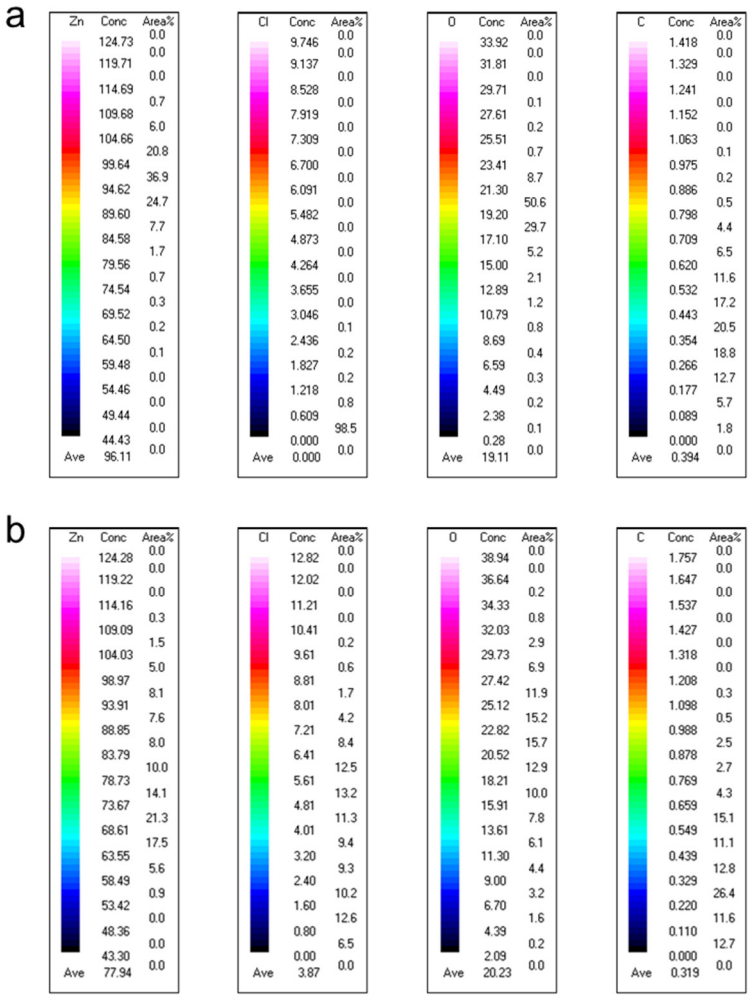

Fig. S18. The concentration and distribution of Zn, Cl, O, and C on the Zn surface after initial stripping with **(a)** BE and **(b)** 2H8D electrolyte (EPMA/WDS results).

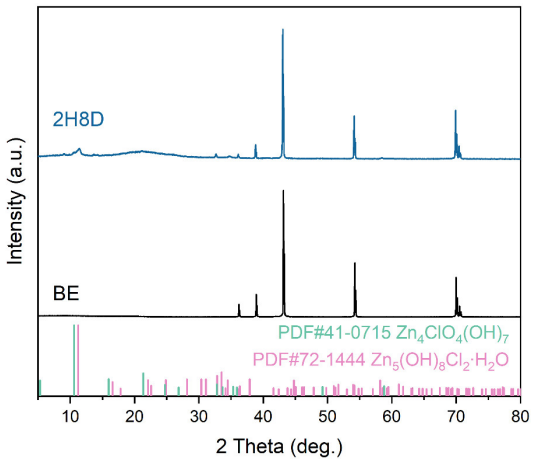

Fig. S19. XRD patterns of the Zn surface after initial stripping in the BE and 2H8D electrolytes.

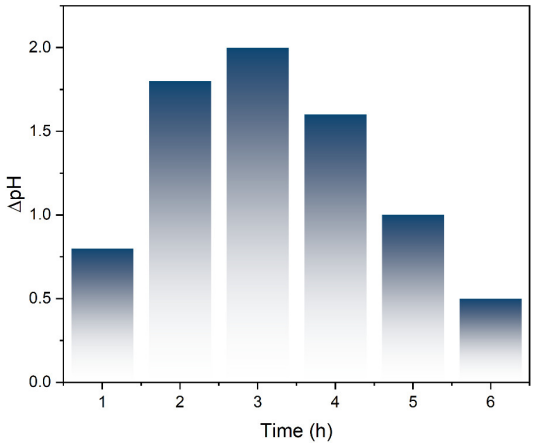

Fig. S20. Difference in pH per hour of 2H8D electrolyte near the IS-Zn electrode in Zn||Zn cell.

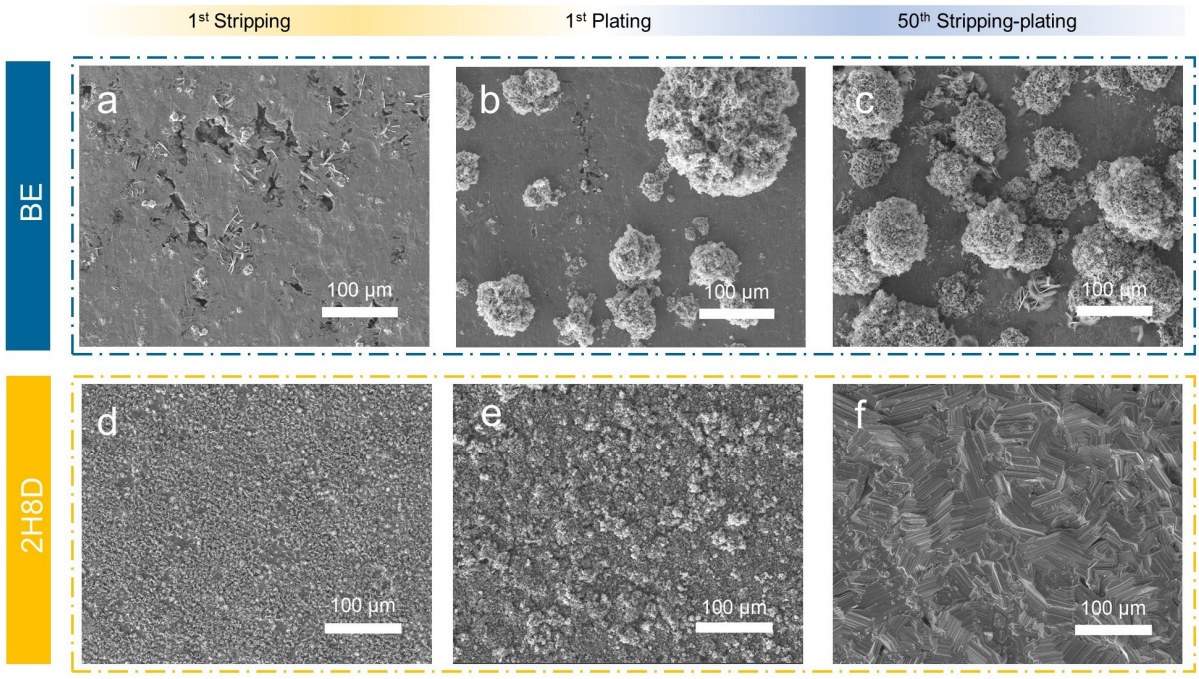

Fig. S21. SEM images of Zn foil after first stripping, first plating, and fiftieth plating at 2 mA cm^{-2} and 1 mAh cm^{-2} in **(a–c)** BE and **(d–f)** 2H8D electrolytes.

The IS-Zn electrode displays a spongy dendrite surface in the BE electrolyte after 50 cycles, whereas the electrode using 2H8D exhibits a tightly packed crystalline mosaic.

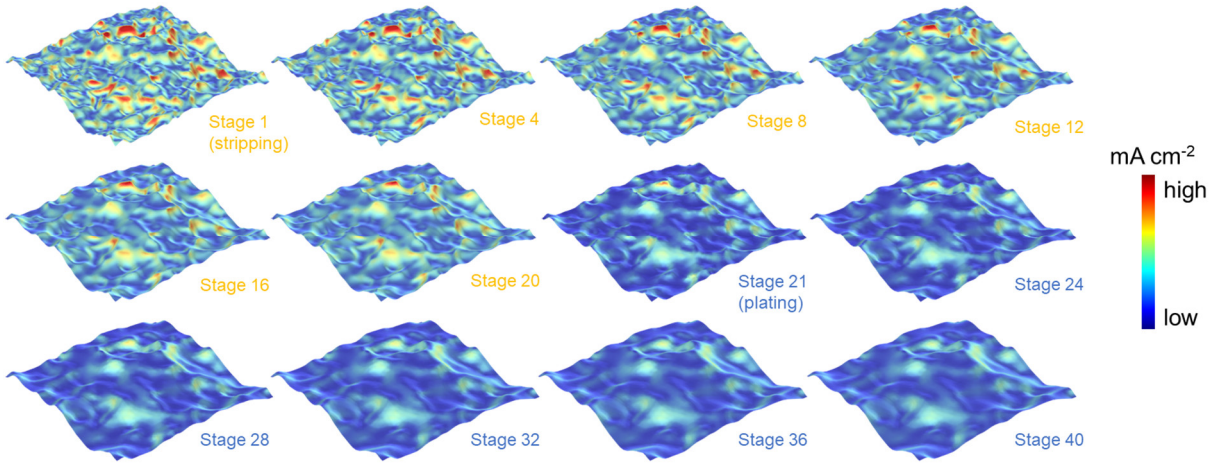

Fig. S22. Electric field on Zn anode in BE electrolyte during stripping/plating process.

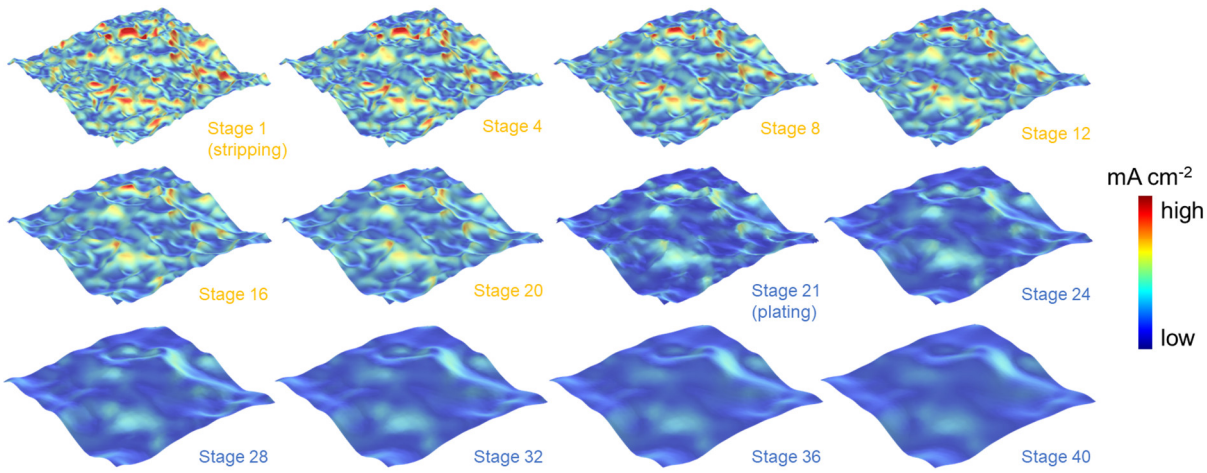

Fig. S23. Electric field on Zn anode in 2H8D electrolyte during stripping/plating process.

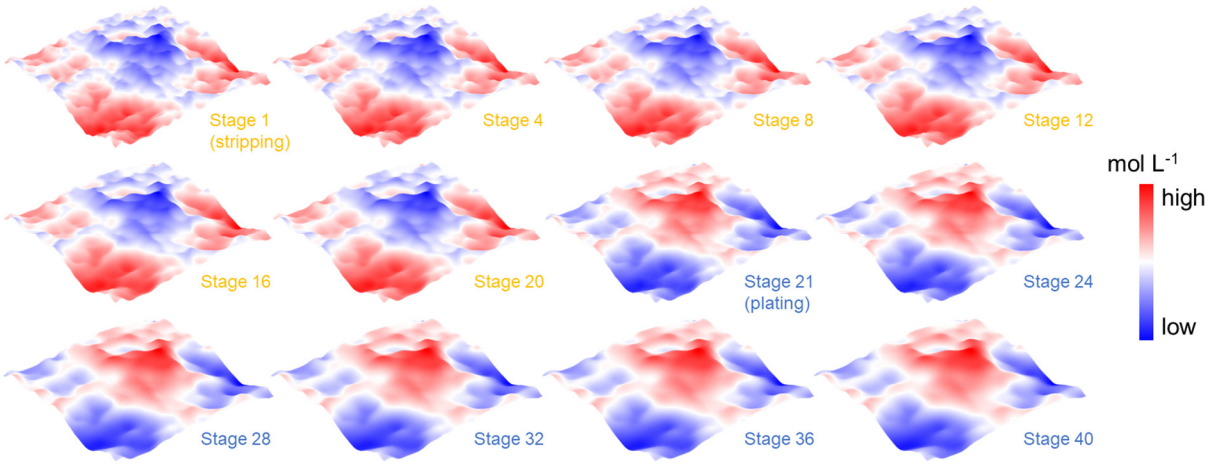

Fig. S24. Zn^{2+} concentration field on Zn anode in BE electrolyte during stripping/plating process.

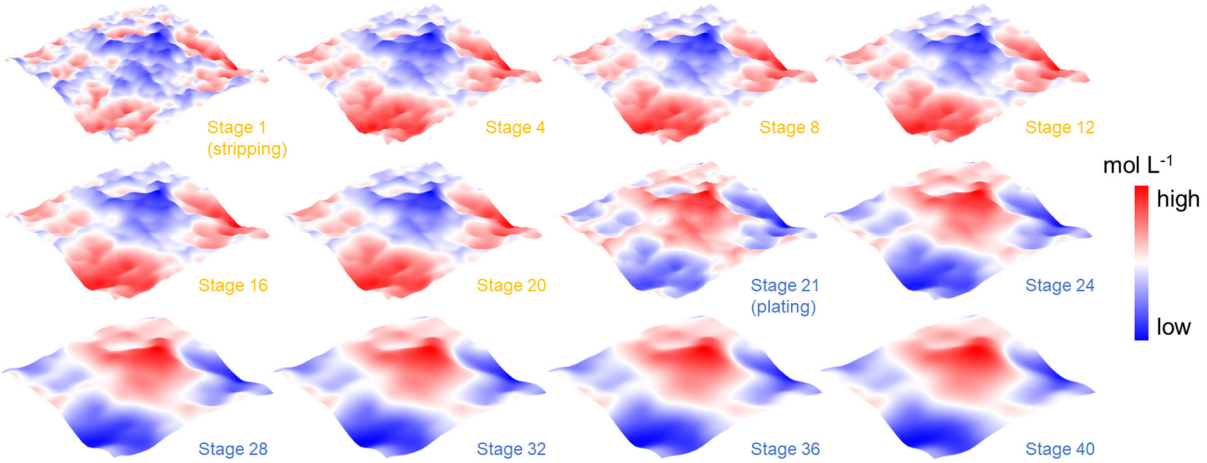

Fig. S25. Zn^{2+} concentration field on Zn anode in 2H8D electrolyte during stripping/plating process.

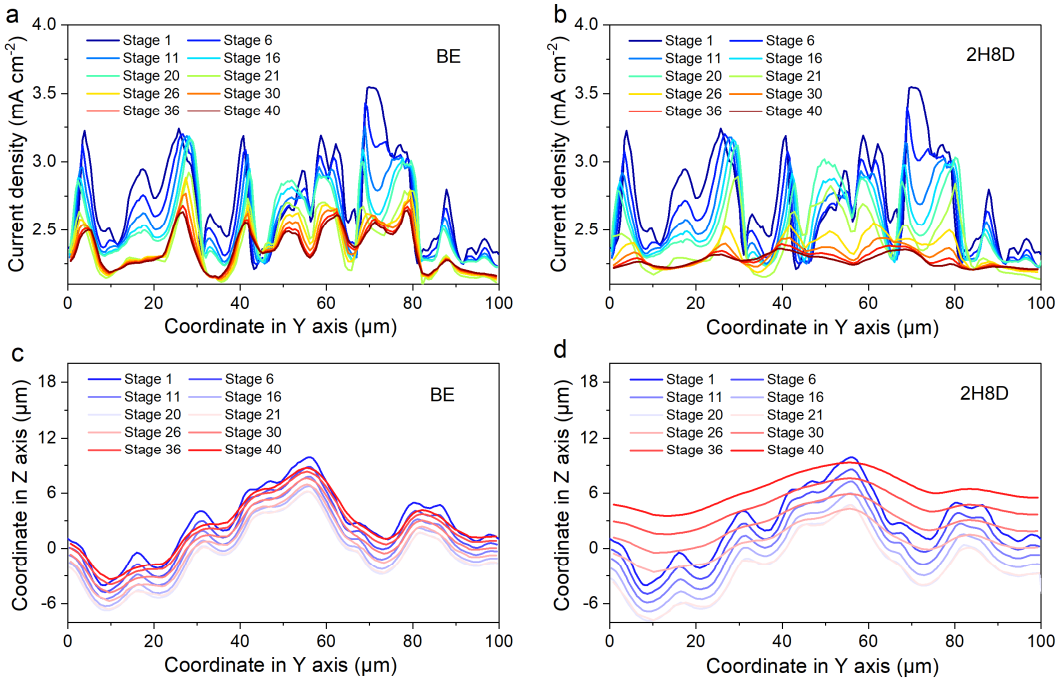

Fig. S26. Variation of current density on Zn anode along Y-axis at X =50 μm in **(a)** BE and **(b)** 2H8D electrolytes. Height profile of Zn anode along with the stripping/plating stage in **(c)** BE and **(d)** 2H8D electrolytes.

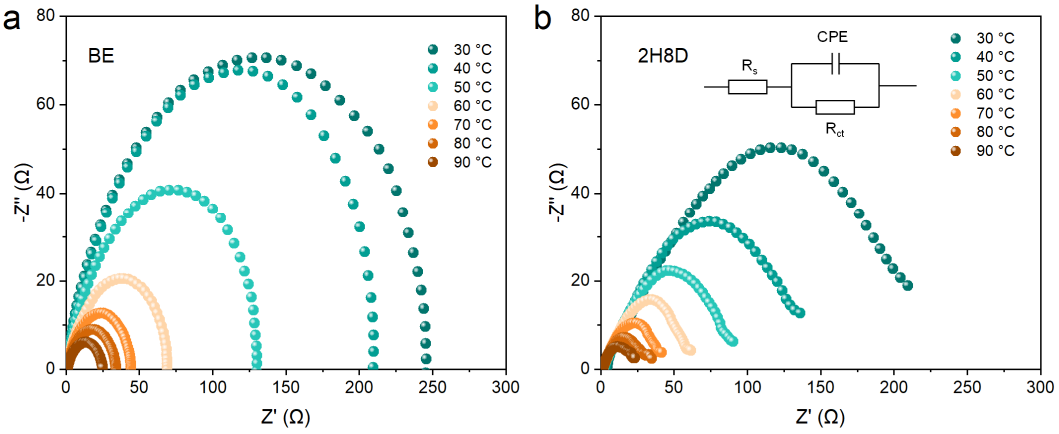

Fig. S27. Temperature-dependent electrochemical impedance spectra of Zn||Zn cells with **(a)** BE and **(b)** 2H8D electrolytes.

To elaborate on the Zn^{2+} desolvation behavior, EIS at different temperatures from 30 to 90 ºC was measured. The activation energy was calculated by the following equation:

$$\frac{1}{R_{ct}} = A\exp(-\frac{E_a}{RT})$$

where E_a is the activation energy, R_{ct} is the interfacial resistance, A is the pre-exponential factor, R is the gas constant, and T is temperature.

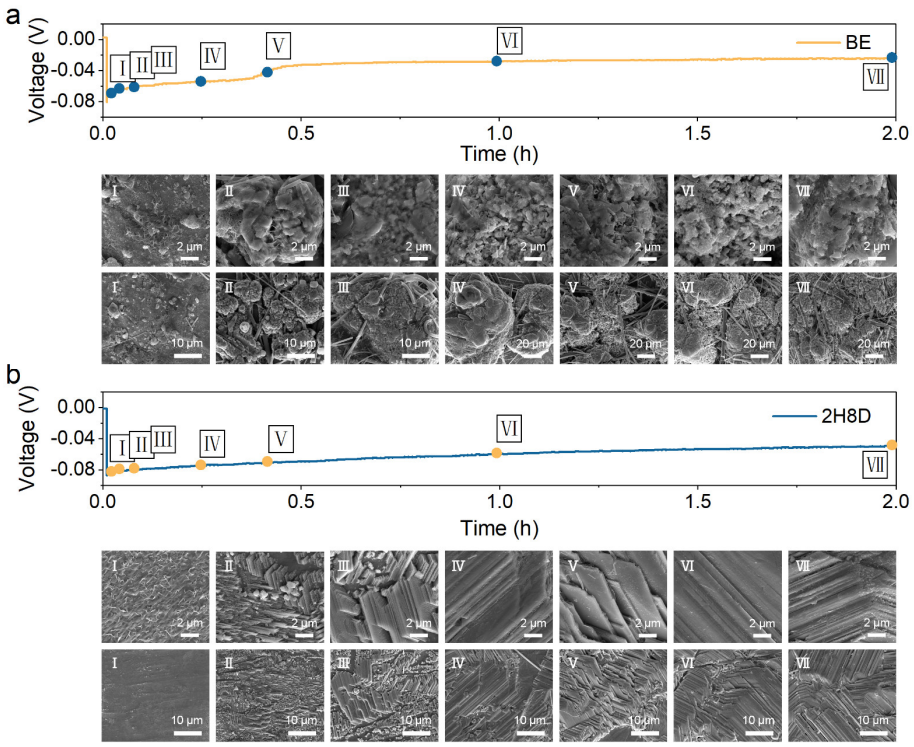

Fig. S28. SEM images of Zn electrodes during first plating at 1 mA cm^{-2} and 2 mAh cm^{-2} in **(a)** BE and **(b)** 2H8D electrolytes.

When the Zn foil is plated at 1 mA cm^{-2} for one minute, uneven nucleation is exhibited on the Zn surface in the BE electrolyte, which is attributed to uneven electric field intensity and ionic fluxes at the interface. As the electrodeposition time is extended, dendrites are gradually formed and accumulated. Large and protruding clusters are observed on Zn surfaces. Conversely, uniform nucleation and growth are exhibited in the 2H8D electrolyte. As the plating time is increased, the plated Zn adheres tightly to the Zn surface, forming a smooth layer.

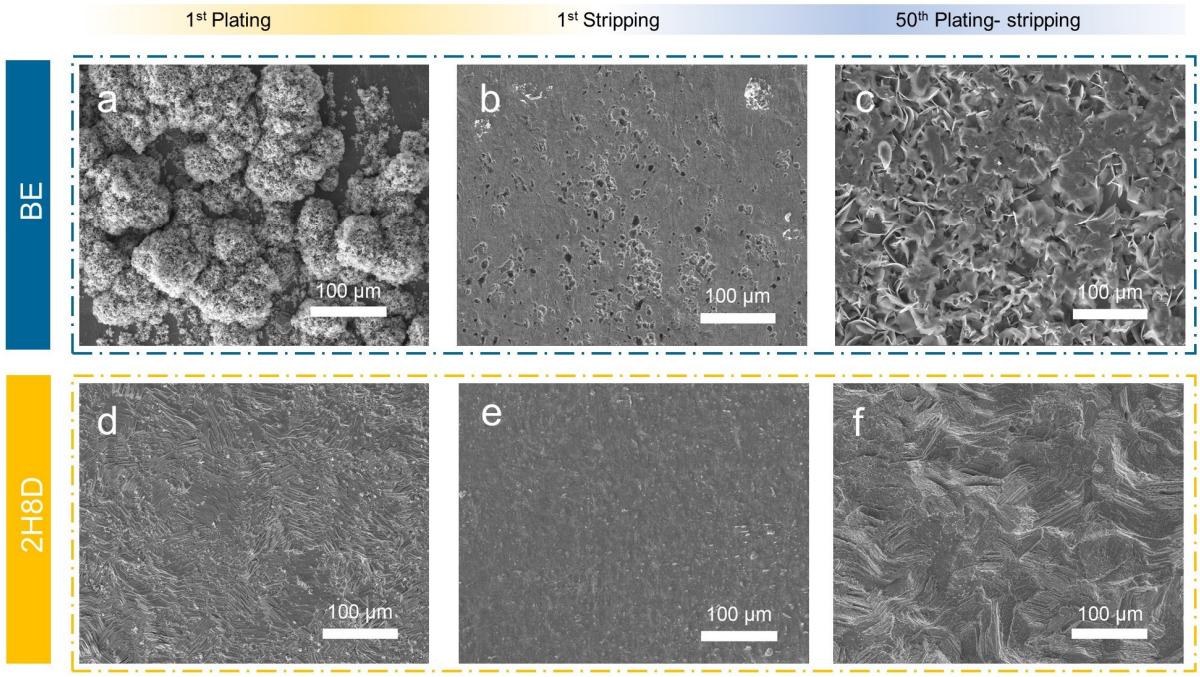

Fig. S29. SEM images of Zn electrodes after first plating, first stripping, and fiftieth stripping at 2 mA cm^{-2} and 1 mAh cm^{-2} in **(a–c)** BE and **(d–f)** 2H8D electrolytes.

In the BE electrolyte, the initial plated Zn electrode even plated on flat electrodes forms dendrites. After 50 cycles, the size and depth of the pits from stripping are enlarged. In contrast, electrodes using the 2H8D electrolyte can be reversible in stripping/plating.

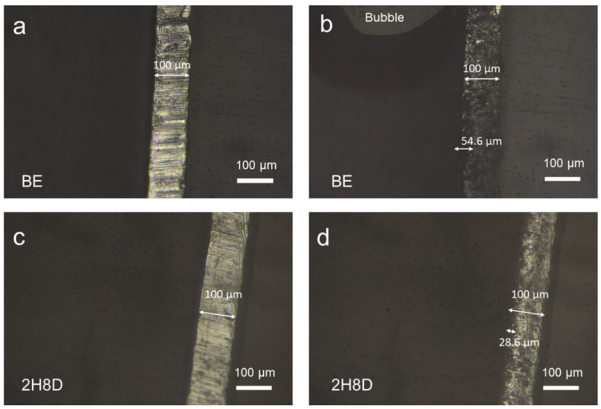

Fig. S30. *In-situ* optical observations of Zn electrodes before and after three stripping/plating cycles at 5 mA cm^{-2} in the **(a, b)** BE and **(c, d)** 2H8D electrolytes.

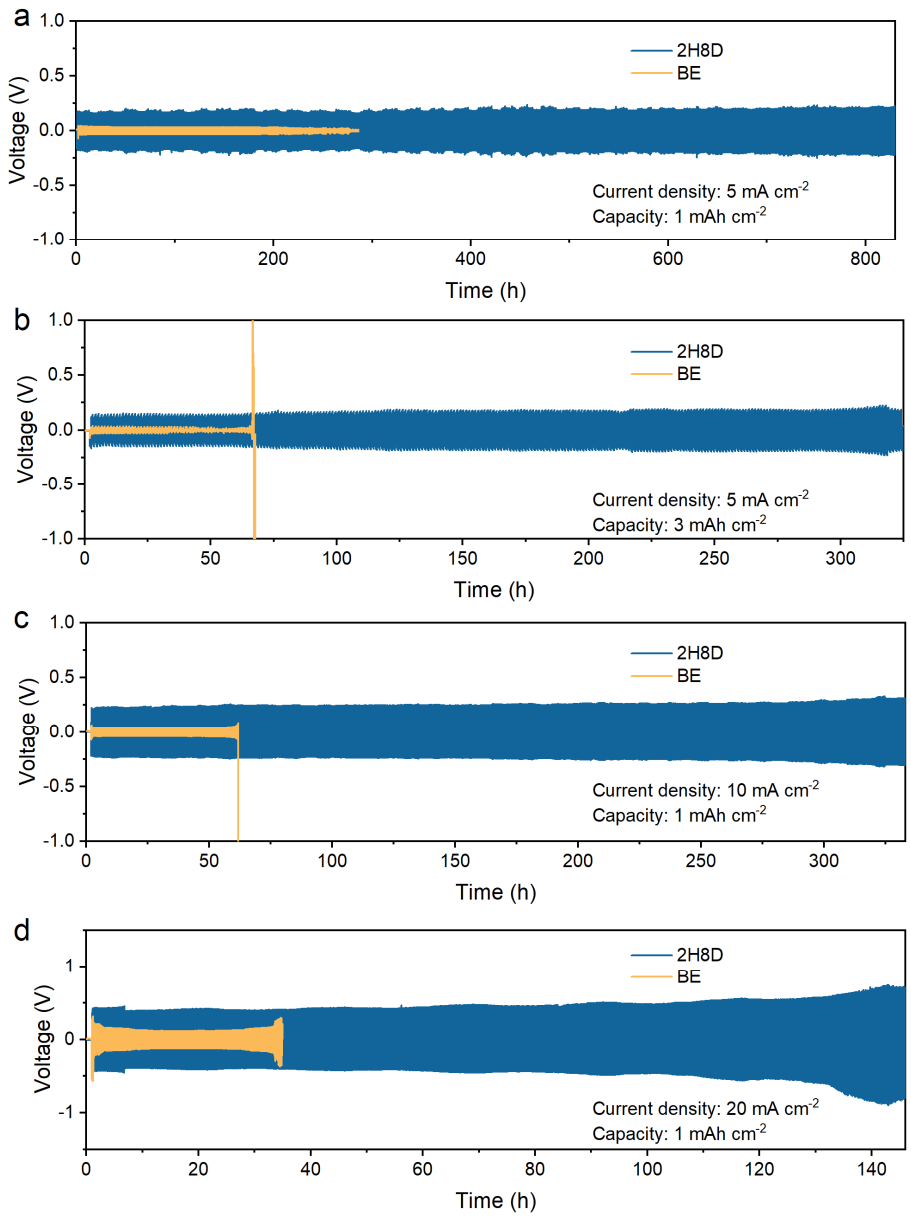

Fig. S31. Cycling stability of Zn||Zn symmetric cells with BE and 2H8D electrolyte at different current conditions: **(a)** 5 mA cm^{-2}, 1 mAh cm^{-2}, **(b)** 5 mA cm^{-2}, 3 mAh cm^{-2}, **(c)** 10 mA cm^{-2}, 1 mAh cm^{-2}, and **(d)** 20 mA cm^{-2}, 1 mAh cm^{-2}.

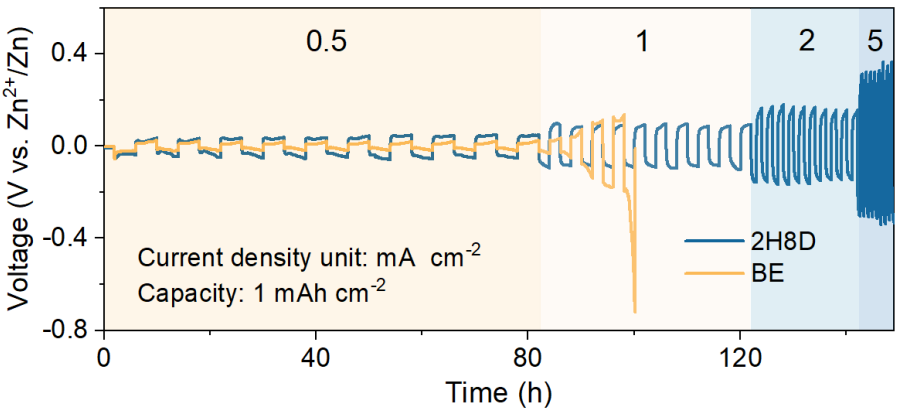

Fig. S32. Rate performance of Zn||Zn symmetric cells with BE and 2H8D electrolytes. The current density varies from 0.5, 1, 2 to 5 mA cm^{-2} per 10 cycles with a discharge depth fixed at 1 mAh cm^{-2}.

The cell using 2H8D electrolyte exhibits stable voltage hysteresis when current densities are increased from 0.5 mA cm^{-2} to 5 mA cm^{-2} with 1 mAh cm^{-2}, respectively. In contrast, the overpotential increased sharply for the cell using BE electrolyte at 1 mA cm^{-2}.

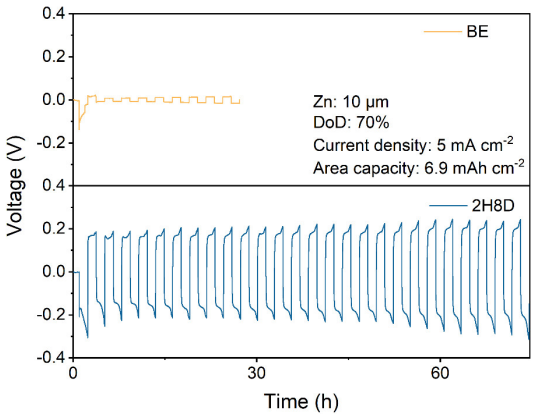

Fig. S33. Cycling stability of Zn||Zn symmetric cells with BE and 2H8D electrolyte at 5 mA cm^{-2} and 6.9 mAh cm^{-2}.

The symmetric cell with 2H8D electrolyte shows a prolonged lifespan of 75 hours even under the severe depth of discharge (DoD: 70%). In contrast, the cell used BE electrolyte only lasted 5 hours at a current density of 5 mA cm^{-2} with a capacity of 6.9 mAh cm^{-2}.

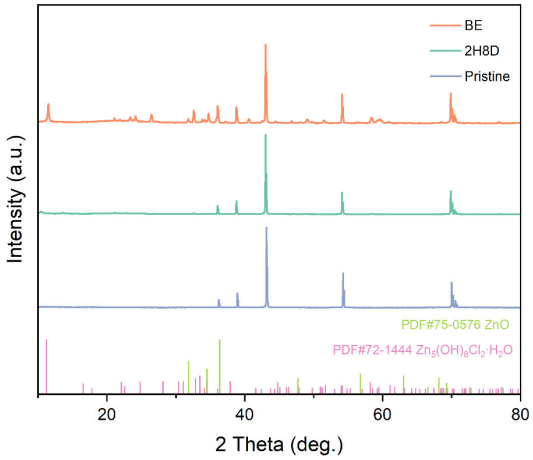

Fig. S34. XRD patterns of Zn anode in BE and 2H8D electrolytes after 100 cycles.

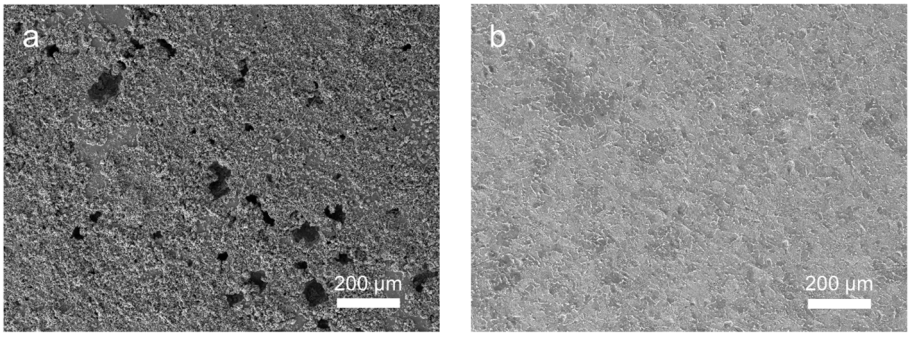

Fig. S35. SEM images of Zn electrode after 100 cycles at 1 mA cm^{-2} and 1 mAh cm^{-2} in **(a)** BE and **(b)** 2H8D electrolytes.

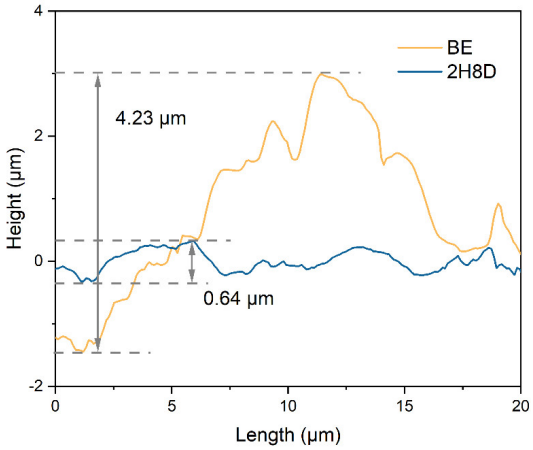

Fig. S36. Height profile of the AFM images diagonal.

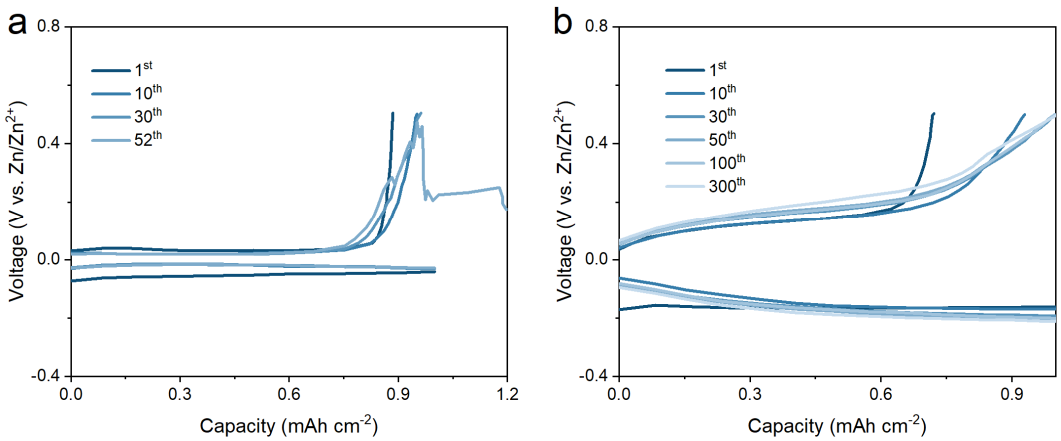

Fig. S37. Voltage profiles of Zn||Ti cells using **(a)** BE and **(b)** 2H8D electrolytes after different cycles at 5 mA cm^{-2} and 1 mAh cm^{-2}.

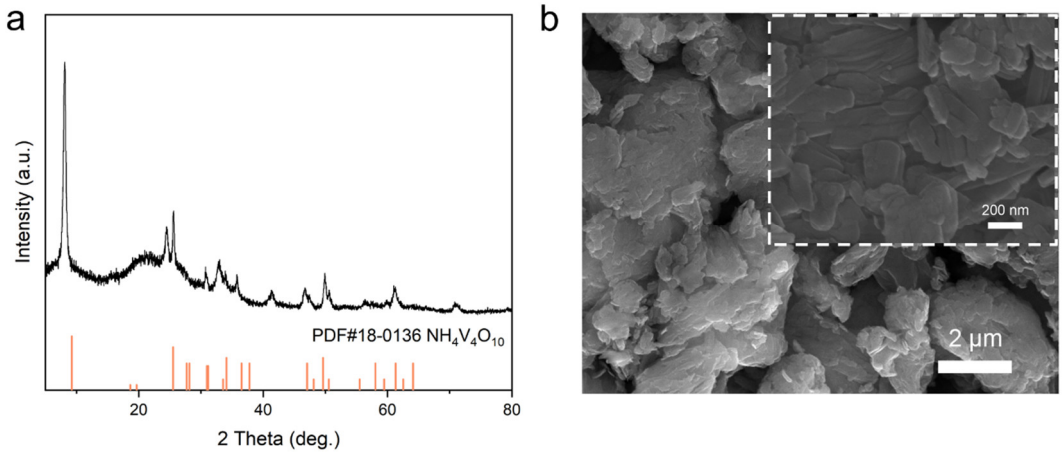

Fig. S38. (a) XRD pattern and **(b)** SEM images of as-prepared $NH_4V_4O_{10}$.

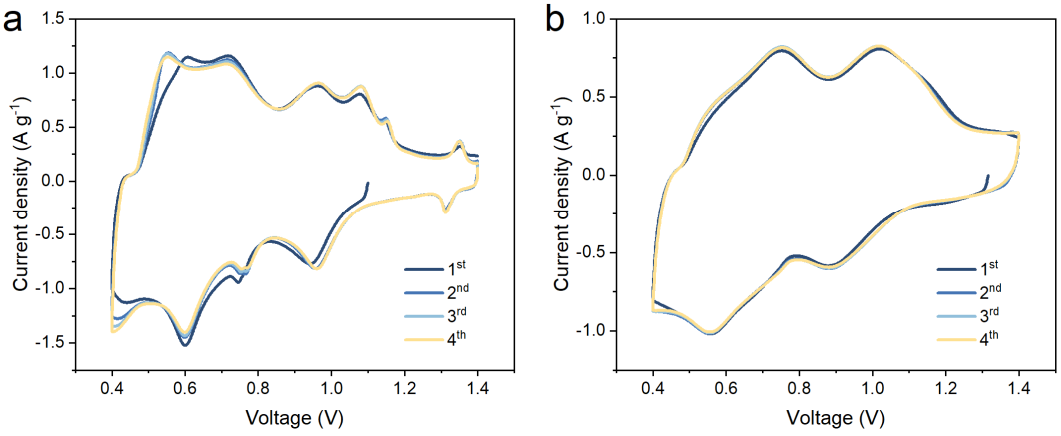

Fig. S39. CV curves of $NH_4V_4O_{10}$||Zn full cells at 0.5 mV s^{-1} in **(a)** BE and **(b)** 2H8D electrolytes.

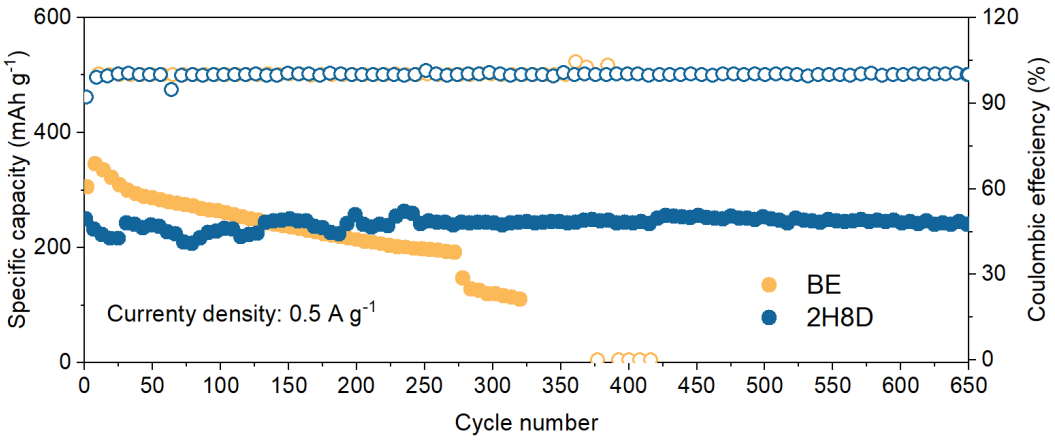

Fig. S40. Cycling performance of $NH_4V_4O_{10}$||Zn cells at 0.5 A g^{-1} in BE and 2H8D electrolytes.

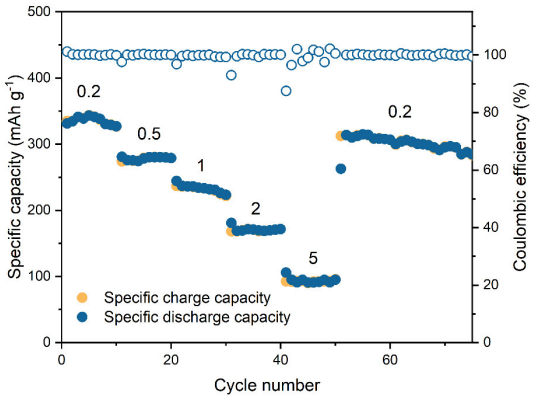

Fig. S41. Rate performance of $NH_4V_4O_{10}$||Zn cell at different current densities from 0.2 to 5 A g^{-1}.

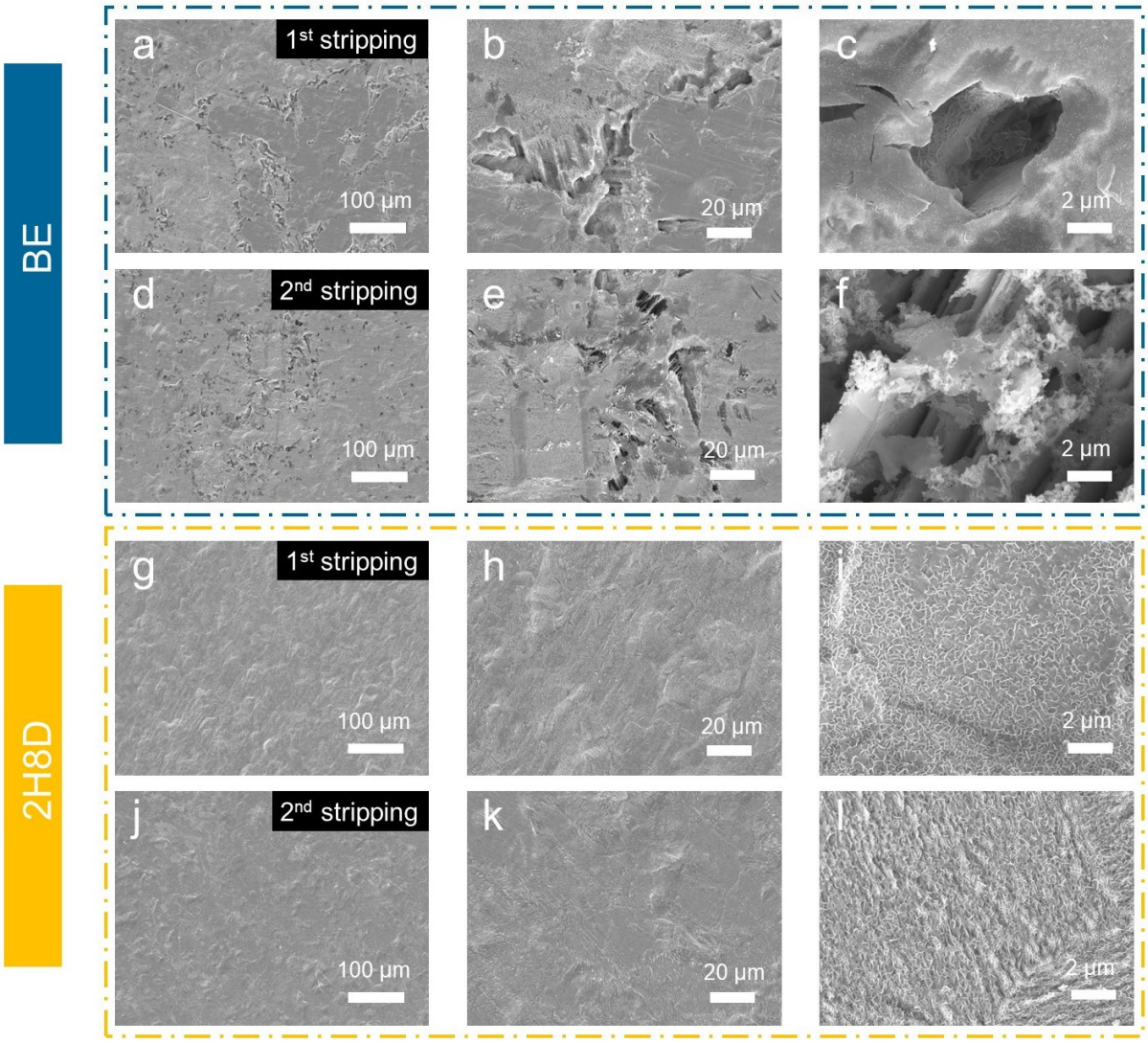

Fig. S42. SEM images of Zn dissembled from $NH_4V_4O_{10}$||Zn full cells after first stripping and second stripping at 5 A g^{-1} in **(a−f)** BE and **(g−l)** 2H8D electrolytes.

For the first stripping of the Zn anode, the buffer SEI can be observed in the 2H8D electrolyte, whereas the stripping behavior in the BE electrolyte is inhomogeneous. The deep pits on the Zn surface further deteriorate in the following stripping.

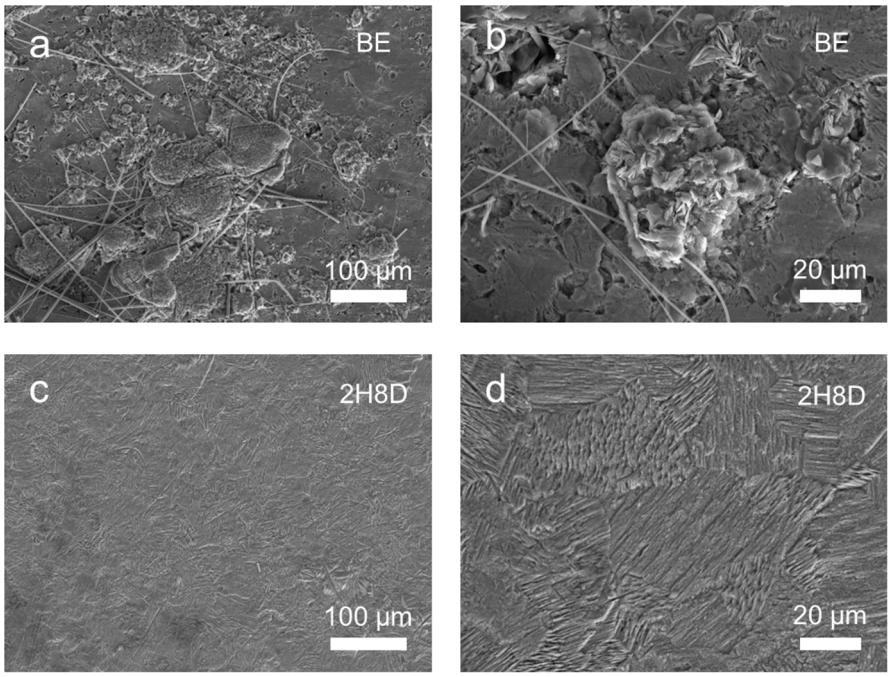

Fig. S43. SEM images of Zn anode dissembled from $NH_4V_4O_{10}$||Zn full cells after 500 cycles at 5 A g^{-1} in **(a, b)** BE and **(c, d)** 2H8D electrolytes.

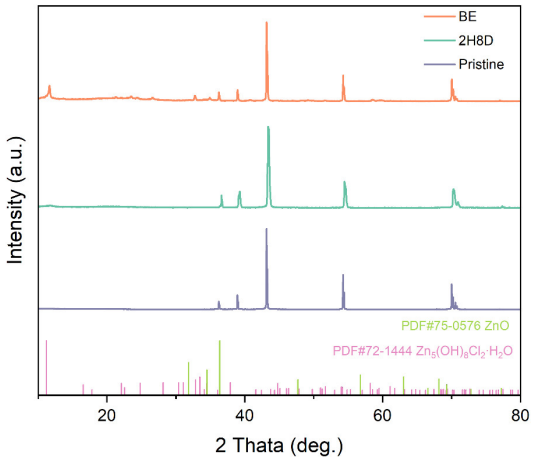

Fig. S44. The XRD patterns of the Zn anode dissembled from $NH_4V_4O_{10}$||Zn full cells after 500 cycles at 5 A g^{-1} in BE and 2H8D electrolytes.

Undesired insulating by-products are detected on the surface of the Zn anode from XRD patterns, which indicates enhanced thermodynamic stability of 2H8D electrolyte against Zn metal as compared with BE electrolyte.

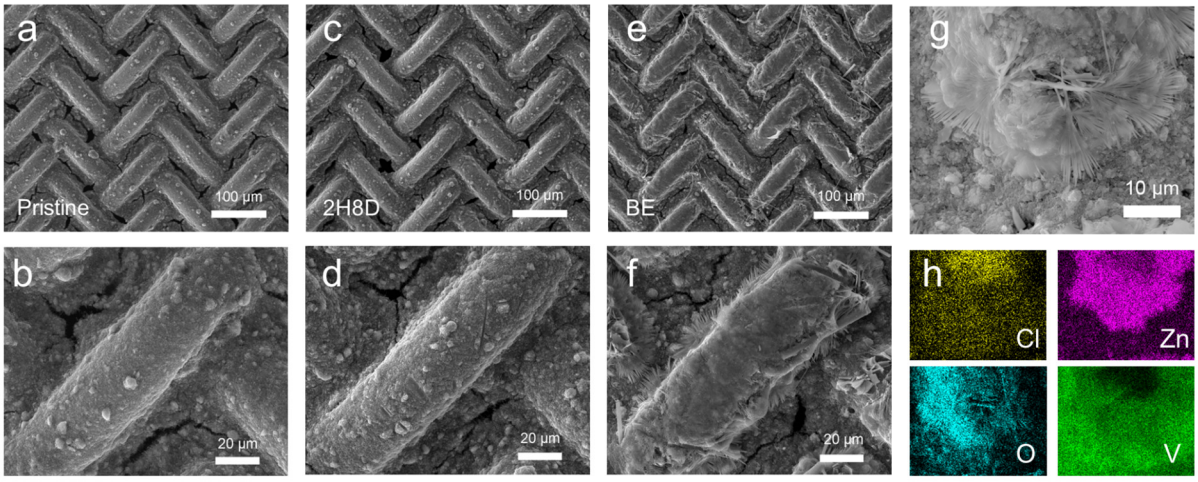

Fig. S45. SEM images of **(a, b)** prepared $NH_4V_4O_{10}$ cathode before cycle, $NH_4V_4O_{10}$ cathode dissembled from $NH_4V_4O_{10}$||Zn full cells after 500 cycles at 5 A g^{-1} in (**c, d)** 2H8D and **(e, f)** BE electrolytes. **(g, h)** EDS mapping images of $NH_4V_4O_{10}$ cathode in BE electrolyte after 500 cycles.

Undesired by-products are detected on the surface of the $NH_4V_4O_{10}$ cathode in the BE electrolyte, which indicates enhanced stability of the cathode in the 2H8D electrolyte.

Table S1. Comparison of cyclic reversibility for Zn anode in the recent reports.

Electrolyte/Anode Modification	Current density (mA cm^{-2})	Capacity (mAh cm^{-2})	CPC (mAh cm^{-2})	Ref.
1 M $ZnSO_4$+ sodium anthraquinone-2-sulfonate (AQS)	0.5	0.5	1250	[23]
2 M $ZnSO_4$+ diethylene glycol monomethyl ether (DGME)	0.5	0.25	1500	[24]
2 M $ZnSO_4$+ propylene glycol (PG)	0.5	0.5	1750	[25]
1 M $Zn(OAc)_2$+ formamide (FA)	1	1	580	[26]
graphene quantum dots (GQDs)-Zn	1	1	1200	[27]
1 M $ZnSO_4$+ tetraphenylporphyrin tetrasulfonic acid (TPPS)	1	1	2250	[28]
1 M $ZnSO_4$+ glucose	5	5	275	[29]
3 M $Zn(CF_3SO_3)_2$+ trimethyl phosphate (TMP)	1	1	2000	[30]
TiN(200)@Zn	5	0.5	2500	[31]
Zn@CuNW	5	2.5	1250	[32]
MXene-mPPy/Zn	0.2	0.2	500	[33]
This work	1	1	6186	
This work	5	1	4155	
This work	5	3	1625	
This work	10	1	3330	
This work	20	1	2920	

Table S2. Comparison of the electrochemical stability of $NH_4V_4O_{10}$||Zn cell with different electrolyte and anode.

Electrolyte	Cathode||Anode	Current density (mAh g^{-1})	Cycle number	Capacity retention (%)	Ref.
2 M $ZnSO_4$+ gelatin gel electrolyte	$NH_4V_4O_{10}$||ss-ZnP	0.5	250	54	[34]
2.9 m $Zn(ClO_4)_2$−$CO(NH_2)_2$−H_2O	$NH_4V_4O_{10}$||Zn	1	100	57	[35]
2 M $ZnSO_4$+ fluoroethylene carbonate (FEC)	O_d-$NH_4V_4O_{10}$||Zn	5	700	64.4	[36]
2 M $ZnSO_4$	$NH_4V_4O_{10}$||Zn@FCDs	1	500	66	[37]
2 M $ZnSO_4$	$NH_4V_4O_{10}$||HEO-CNFs	10	5000	71.06	[38]
2 M $ZnSO_4$+ (aminomethyl) phosphonic acid (AMPA)	$NH_4V_4O_{10}$||Zn	2	1000	67	[39]
2 M $ZnSO_4$+ ethylene diamine tetraacetic acid (EDTA)	$NH_4V_4O_{10}$||Zn	2	800	68.3	[40]
2 M $Zn(CF_3SO_3)_2$+ ethylene glycol	$NH_4V_4O_{10}$||Zn	0.5	300	75	[41]
2 M $ZnSO_4$+ ectoine (ET)	$NH_4V_4O_{10}$||Zn	0.5	200	80.1	[42]
2 M $ZnSO_4$	$NH_4V_4O_{10}$||Zn-Ti	5	4000	80	[43]
2 M $ZnSO_4$	$NH_4V_4O_{10}$||BTO/PVT@Zn	4	2000	79	[44]
2 M $ZnSO_4$+ Trimethyl phosphate (TMP)	$NH_4V_4O_{10}$||Zn	5	1500	84.5	[45]
2 M $ZnSO_4$+ NH_4OAc	O_d-$NH_4V_4O_{10}$||Zn	1	500	83.7	[46]
2 M $Zn(OTf)_2$+ Hexamethylphosphoramide (HMPA)	$NH_4V_4O_{10}$||Zn	1	1000	88.7	[47]
This work	$NH_4V_4O_{10}$||Zn	0.5	650	96.48	

This work	$NH_4V_4O_{10}$||Zn	5	5000	84.67

References

1. Y. Liu, X. Xu, M. Sadd, O. O. Kapitanova, V. A. Krivchenko, J. Ban, J. Wang, X. Jiao, Z. Song, J. Song, S. Xiong and A. Matic, *Adv. Sci.*, 2021, **8**, 2003301.
2. X. Xu, Y. Liu, J.-Y. Hwang, O. O. Kapitanova, Z. Song, Y.-K. Sun, A. Matic and S. Xiong, *Adv. Energy Mater.*, 2020, **10**, 2002390.
3. X. Jiao, X. Wang, X. Xu, Y. Wang, H.-H. Ryu, J. Park, J.-Y. Hwang, S. Xiong, Y.-K. Sun, Z. Song and Y. Liu, *Adv. Energy Mater.*, 2023, **13**, 2301708.
4. B. Li, P. Ruan, X. Xu, Z. He, X. Zhu, L. Pan, Z. Peng, Y. Liu, P. Zhou, B. Lu, L. Dai and J. Zhou, *Nano-Micro Lett.*, 2024, **16**, 76.
5. G. Kresse and J. Hafner, *Phys. Rev. B*, 1994, **49**, 14251-14269.
6. G. Kresse and J. Furthmüller, *Comput. Mater. Sci*, 1996, **6**, 15-50.
7. P. E. Blöchl, O. Jepsen and O. K. Andersen, *Phys. Rev. B*, 1994, **49**, 16223-16233.
8. G. Kresse and D. Joubert, *Phys. Rev. B*, 1999, **59**, 1758-1775.
9. J. P. Perdew, K. Burke and M. Ernzerhof, *Phys. Rev. Lett.*, 1996, **77**, 3865-3868.
10. E. Caldeweyher, C. Bannwarth and S. Grimme, *J. Chem. Phys.*, 2017, **147**, 034112.
11. E. R. Johnson and A. D. Becke, *J. Chem. Phys.*, 2005, **123**, 024101.
12. J. Zheng, X. Xu and D. G. Truhlar, *Theor. Chem. Acc.*, 2011, **128**, 295-305.
13. W. Humphrey, A. Dalke and K. Schulten, *J. Mol. Graphics*, 1996, **14**, 33-38.
14. A. P. Thompson, H. M. Aktulga, R. Berger, D. S. Bolintineanu, W. M. Brown, P. S. Crozier, P. J. in 't Veld, A. Kohlmeyer, S. G. Moore, T. D. Nguyen, R. Shan, M. J. Stevens, J. Tranchida, C. Trott and S. J. Plimpton, *Comp Phys Commun*, 2022, **271**, 108171.
15. G. A. Kaminski, R. A. Friesner, J. Tirado-Rives and W. L. Jorgensen, *J. Phys. Chem. B*, 2001, **105**, 6474-6487.
16. M. Schauperl, P. S. Nerenberg, H. Jang, L.-P. Wang, C. I. Bayly, D. L. Mobley and M. K. Gilson, *Commun. Chem.*, 2020, **3**, 44.
17. J. Zhang and T. Lu, *Phys. Chem. Chem. Phys.*, 2021, **23**, 20323-20328.
18. L. Martínez, R. Andrade, E. G. Birgin and J. M. Martínez, *J. Comput. Chem.*, 2009, **30**, 2157-2164.
19. A. I. Jewett, D. Stelter, J. Lambert, S. M. Saladi, O. M. Roscioni, M. Ricci, L. Autin, M. Maritan, S. M. Bashusqeh, T. Keyes, R. T. Dame, J.-E. Shea, G. J. Jensen and D. S. Goodsell, *JMB*, 2021, **433**, 166841.
20. Z. Cai, J. Wang, Z. Lu, R. Zhan, Y. Ou, L. Wang, M. Dahbi, J. Alami, J. Lu, K. Amine and Y. Sun, *Angew. Chem. Int. Ed.*, 2022, **61**, e202116560.
21. D. Xiao, Q. Li, D. Luo, R. Gao, Z. Li, M. Feng, T. Or, L. Shui, G. Zhou, X. Wang and Z. Chen, *Adv. Funct. Mater.*, 2021, **31**, 2011109.
22. C. Yan, H.-R. Li, X. Chen, X.-Q. Zhang, X.-B. Cheng, R. Xu, J.-Q. Huang and Q. Zhang, *J. Am. Chem. Soc.*, 2019, **141**, 9422-9429.
23. R. Sun, D. Han, C. Cui, Z. Han, X. Guo, B. Zhang, Y. Guo, Y. Liu, Z. Weng and Q.-H. Yang, *Angew. Chem. Int. Ed.*, 2023, **62**, e202303557.
24. B. Xie, Q. Hu, X. Liao, X. Zhang, H. Lang, R. Zhao, Q. Zheng, Y. Huo, J. Zhao, D. Lin and X.-L. Wu, *Adv. Funct. Mater.*, 2024, **34**, 2311961.
25. J. Li, S. Zhou, Y. Chen, X. Meng, A. Azizi, Q. He, H. Li, L. Chen, C. Han and A. Pan, *Adv. Funct. Mater.*, 2023, **33**, 2307201.
26. C. You, R. Wu, X. Yuan, J. Ye, L. Liu, L. Fu, P. Han and Y. Wu, *Energy Environ. Sci.*,

2023, **16**, 5096-5107.
27. Y.-F. Li, R. Jiao, X.-Y. Shen, Y.-H. Song, L. Ding, G.-D. Yang, C. Shao, X.-L. Wu, J.-P. Zhang, M.-X. Deng, S.-L. Wang and H.-Z. Sun, *Energy Storage Mater.*, 2023, **62**, 102934.
28. X. Zhao, Y. Wang, C. Huang, Y. Gao, M. Huang, Y. Ding, X. Wang, Z. Si, D. Zhou and F. Kang, *Angew. Chem. Int. Ed.*, 2023, **62**, e202312193.
29. P. Sun, L. Ma, W. Zhou, M. Qiu, Z. Wang, D. Chao and W. Mai, *Angew. Chem. Int. Ed.*, 2021, **60**, 18247-18255.
30. T. Zhang, J. Yang, H. Wang, H. Yu, Q. Li, L. Chen, Y. Chen and T. Wang, *Energy Storage Mater.*, 2024, **65**, 103085.
31. J. Zheng, Z. Cao, F. Ming, H. Liang, Z. Qi, W. Liu, C. Xia, C. Chen, L. Cavallo, Z. Wang and H. N. Alshareef, *ACS Energy Lett.*, 2021, **7**, 197-203.
32. S. Xie, Y. Li, X. Li, Y. Zhou, Z. Dang, J. Rong and L. Dong, *Nano-Micro Lett.*, 2022, **14**, 39.
33. Y. Zhang, Z. Cao, S. Liu, Z. Du, Y. Cui, J. Gu, Y. Shi, B. Li and S. Yang, *Adv. Energy Mater.*, 2022, **12**, 2103979.
34. C. Cao, K. Zhou, W. Du, C. C. Li, M. Ye, Y. Zhang, Y. Tang and X. Liu, *Adv. Energy Mater.*, 2023, **13**, 2301835.
35. Z. Wang, J. Diao, J. N. Burrow, K. K. Reimund, N. Katyal, G. Henkelman and C. B. Mullins, *Adv. Funct. Mater.*, 2023, **33**, 2304791.
36. D. Xie, Y. Sang, D. H. Wang, W. Y. Diao, F. Y. Tao, C. Liu, J. W. Wang, H. Z. Sun, J. P. Zhang and X. L. Wu, *Angew. Chem. Int. Ed. Engl.*, 2022, **62**, e202216934.
37. Z. Ge, L. Xu, Y. Xu, J. Wu, Z. Geng, X. Xiao, W. Deng, G. Zou, H. Hou and X. Ji, *Nano Energy*, 2024, **119**, 109053.
38. Y. Li, H. Jia, U. Ali, H. Wang, B. Liu, L. Li, L. Zhang and C. Wang, *Adv. Energy Mater.*, 2023, **13**, 2301643.
39. J. Zhang, P. Li, Y. Wang, Z. Zhao and Z. Peng, *Adv. Funct. Mater.*, 2023, **33**, 2305804.
40. R. Meng, H. Li, Z. Lu, C. Zhang, Z. Wang, Y. Liu, W. Wang, G. Ling, F. Kang and Q. H. Yang, *Adv. Mater.*, 2022, **34**, 2200677.
41. R. Chen, C. Zhang, J. Li, Z. Du, F. Guo, W. Zhang, Y. Dai, W. Zong, X. Gao, J. Zhu, Y. Zhao, X. Wang and G. He, *Energy Environ. Sci.*, 2023, **16**, 2540-2549.
42. Q. Meng, Q. Bai, R. Zhao, P. Cao, G. Zhang, J. Wang, F. Su, X. Zhou, J. Yang and J. Tang, *Adv. Energy Mater.*, 2023, **13**, 2302828.
43. Y. Zhao, S. Guo, M. Chen, B. Lu, X. Zhang, S. Liang and J. Zhou, *Nat. Commun.*, 2023, **14**, 7080.
44. Q. Zong, B. Lv, C. Liu, Y. Yu, Q. Kang, D. Li, Z. Zhu, D. Tao, J. Zhang, J. Wang, Q. Zhang and G. Cao, *ACS Energy Lett.*, 2023, **8**, 2886-2896.
45. X. Luo, M. Zhou, Z. Luo, T. Shi, L. Li, X. Xie, Y. Sun, X. Cao, M. Long, S. Liang and G. Fang, *Energy Storage Mater.*, 2023, **57**, 628-638.
46. D. Han, Z. Wang, H. Lu, H. Li, C. Cui, Z. Zhang, R. Sun, C. Geng, Q. Liang, X. Guo, Y. Mo, X. Zhi, F. Kang, Z. Weng and Q. H. Yang, *Adv. Energy Mater.*, 2022, **12**, 2102982.
47. Z. Huang, Z. Li, Y. Wang, J. Cong, X. Wu, X. Song, Y. Ma, H. Xiang and Y. Huang, *ACS Energy Lett.*, 2023, **8**, 372-380.